frontiers | Frontiers in Materials

TYPE Original Research
PUBLISHED 08 December 2022
DOI 10.3389/fmats.2022.1088196

OPEN ACCESS

EDITED BY
Seng Hua Lee,
Putra Malaysia University, Malaysia

REVIEWED BY
Dahlang Tahir,
Hasanuddin University, Indonesia
Idza Riati Ibrahim,
Universiti Malaysia Sarawak, Malaysia
Wei Chen Lum,
MARA University of Technology, Malaysia

*CORRESPONDENCE
Bagher Aslibeiki,
b.aslibeiki@tabrizu.ac.ir

SPECIALTY SECTION
This article was submitted to Polymeric and Composite Materials, a section of the journal Frontiers in Materials

RECEIVED 03 November 2022
ACCEPTED 28 November 2022
PUBLISHED 08 December 2022

CITATION
Mahmoodi M, Aslibeiki B, Peymanfar R and Naghshara H (2022), Oleaster seed-derived activated carbon/ferrite nanocomposite for microwave absorption in the X-band range. *Front. Mater.* 9:1088196. doi: 10.3389/fmats.2022.1088196

Oleaster seed-derived activated carbon/ferrite nanocomposite for microwave absorption in the X-band range

Mahsa Mahmoodi[1], Bagher Aslibeiki[1]*, Reza Peymanfar[2,3,4] and Hamid Naghshara[1]

[1]Faculty of Physics, University of Tabriz, Tabriz, Iran, [2]Department of Chemical Engineering, Energy Institute of Higher Education, Saveh, Iran, [3]Iranian Society of Philosophers, Department of Science, Tehran, Iran, [4]Peykareh Enterprise Development Co., Tehran, Iran

Conjugated carbonaceous structures achieved from biological materials were significantly considered electromagnetic wave absorbing materials due to their eye-catching dielectric, lightweight, low-cost, and chemical stability features. To strengthen the microwave absorbing performance of the porous carbon (Oleaster seeds), Fe_3O_4 magnetic nanoparticles have been successfully anchored onto the surface of biomass-derived material through a co-precipitation method. Noticeably, the dielectric constant, impedance matching, permeability, and microwave absorbing capability were improved by changing the carbon content. The optimized Fe_3O_4/activated carbon (AC) illustrated the excellent electromagnetic wave absorption performances with a maximum reflection loss (RL) value of −51.12 dB and an effective absorption bandwidth of ~4 GHz (RL < 10 dB) with a thickness of 1 mm. The promoted microwave absorbing characteristics of Fe_3O_4/AC composites are rooted in improved impedance matching, eddy current loss, natural and exchange resonance, and specific surface area, bringing more polarization loss and multiple reflection and scattering. The presented research shed new light on the fabrication of practical microwave-absorbing materials based on biomass-derived materials with a facile experimental procedure.

KEYWORDS

oleastar seed, activated carbon, ferrite (Fe_3O_4), microwave absorption, biomassderived material

1 Introduction

During the last few years, although the rapid development of electronic equipment has made a convenient life, the electromagnetic waves radiated into the environment are harmful to humans and any living species all over the world (Huang et al., 2016; Li et al., 2018a; Zhang et al., 2021). Moreover, electromagnetic waves deal with various military and civilian fields. Thus, electromagnetic wave absorbing materials are used in many new and advanced routes of safety, stealth, and engineering technologies, such as fighter jets that require reconnaissance missions without intrusion signs, wearable electronic devices

that function to mimic human sensory characteristics, building materials mitigating electromagnetic pollutions, and so on (Gao et al., 2018; Peymanfar et al., 2021a; Keykavous-Amand and Peymanfar, 2021). Accordingly, the discovery of electromagnetic wave-absorbing materials is of vast importance in both military and civilian fields (Pang et al., 2017). Microwave absorbers perform based on permeability, permittivity, and tuned impedance matching deduced from the dissipation mechanism (Zhang et al., 2015a; Zhang et al., 2020a; Fang et al., 2022; Wang et al., 2022; Yang et al., 2022; Wang et al., 2023). In recent years, carbon-based electromagnetic wave absorbing materials and their composites have been under the spotlight as the hotspot due to their considerable electrical conductivity, salient relaxation loss potential, lightweight structure, and vast specific surface area (Guo et al., 2009; Ma et al., 2018; Zhou et al., 2022; Chen et al., 2023; Xie et al., 2023). However, conjugated carbonaceous materials are difficult for mass production in the industrial ways due to their complex synthetic procedures and high preparation costs, so using biomass-derived materials has gained huge attention. They are generally agricultural residues and aquatic plants as well as wood, human, industrial, and animal waste (Wang et al., 2017; Pang et al., 2018; Zhang et al., 2020b). These free and available materials reduce the density of eventual microwave absorbing composite owing to their intrinsic chemical features and porous structures, thus giving the absorbers an additional path for the transmission of electromagnetic waves, leading to multiple reflections, and then improving electromagnetic wave absorption (Zhang et al., 2021). In addition, electron transitions and polarization loss comprising dipole, interfacial, and defect polarization pave the way for energy dissipation of this type of material (Guo et al., 2019a; Wang et al., 2020a). Biomaterials must be pretreated through physical, chemical, thermal, or even biological processes before being converted into carbon-based microwave absorbing materials to improve the carbonization process and performance (Liang et al., 2020). It is well known that the dielectric characteristics of pyrolyzed carbon-based microwave absorbing structures essentially originated from their conjugated structures bringing a facil $\pi \rightarrow \pi^*$ and $n \rightarrow \pi^*$ charge transitions (Peymanfar et al., 2022; Peymanfar and Mirkhan, 2022).

Among all metal oxides, ferrites, as a type of compound consisting of iron oxides and other metals, are of interest due to their magnetic properties and high permeability, good flexibility, as well as excellent chemical and thermal stability (Huang et al., 2014; Mu et al., 2022). At the same time, they also have disadvantages, such as low dielectric properties and high density, declining their microwave absorbing practical applications (Liu et al., 2019). On the other hand, ferrits have exposed low efficient bandwidth and microwave absorption intensity (Xie et al., 2022). Therefore, they have been modified with different dielectric materials to augment the microwave absorbing performance. To elevate microwave absorbing performance, combining the conjugated carbon-based materials with ferrites not only amplifies impedance matching but also promotes microwave attenuation through magnetic losses (Mingdong et al., 2018). Magnetite nanoparticles with a high surface to volume ratio, fast kinetics, strong absorption capacity, high reactivity, and easy synthesis compared to other ferrites were used in this work. Also, when an external magnetic field is applied to them, they quickly bind to each other and act as an easy and cost-effective separation process for their extraction from aqueous solutions. After removing the magnetic field, the nanoparticles lose their magnetic moment and return to their original state. Also, magnetite is one of the materials that absorb a lot of electromagnetic energy at microwave frequencies, and its high electrical resistance reduces the formation of eddy currents (Mathew and Juang, 2007). Moreover, Fe_3O_4 has significant saturation magnetization augmenting permeability based on the natural resonance theory.

In this work to produce nanocomposite was the chemical precipitation method, in which the substance that is soluble in the medium is transformed into an insoluble structure. The chemical deposition process included the steps of nucleation, growth, coagulation, and finally nanoparticles are deposited on carbon. The hetero atoms and dangling bonds existing in the AC act as nucleation centers and dispersing agents enhancing the heterogenous interfaces of the eventual composite, elevating polarization loss and microwave absorption.

Zhou *et al.* have prepared Fe_3O_4/AC composite using a walnut shell as a biomass-derived material. The images of the scanning electron microscope for three weight amounts of iron (III) nitrate 0.50, 0.75, and 1.00 mmol show that the carbonaceous structure activated by zinc chloride has many tiny pores. The minimum RL of Fe_3O_4/AC composite reached −40.3 dB at 17.5 GHz with a thickness of 2.00 mm meanwhile, an efficient bandwidth of 6.6 GHz was gained when the thickness was 2.5 mm, showing that the microwave absorbing performances of Fe_3O_4/AC composites have increased compared to the activated carbon sample, generated from the elevated impedance matching (Qiu et al., 2017; Zhou et al., 2019).

The impedance matching plays a pivotal role in tuning microwave absorbing characteristics. An absorber of electromagnetic waves realizes the best performance when being in proper impedance matching between the environment of the incident waves and the absorbing matrix. The desirable impedance matching causes more incident waves to be propagated in an absorbing medium (Wei et al., 2019). The simultaneous mitigating of the electric and magnetic fields of the passing waves in the absorbing medium increases the amount of absorption (Liang et al., 2019). The impedance matching of the Fe_3O_4/AC composite was improved by modulating the content of Fe_3O_4 nanoparticles in the tailored structure (Yun et al., 2020). Fe_3O_4 nanoparticles present a weak RL, usually less than -8 dB (Sung Lee et al., 2015). $CoFe_2O_4$/C composites were architected by Hong *et al.* using an eggshell membrane as a carbon-based

precursor, carbonized for 1 h at 800°C. The size of carbon pores was between 10 and 200 μm. Also, the RL curve illustrated several notches, which were −35.35, −49.6, and −34.6 dB in thicknesses of 2, 2.5, and 3 mm, respectively. $CoFe_2O_4$/C composites were fabricated at 700°C in an argon atmosphere, showing an RL of −27.9 dB in 2 mm thickness with an efficient bandwidth of 5.5 GHz. The RL value reached −42 dB when the thickness was changed to 3 mm (Gabal et al., 2021).

Porous carbon fibers based on rice husk and its composites were synthesized through a pre-modification and post-modification method by Fang et al. (2017) The obtained hybrid showed the absorption performance of electromagnetic waves with a reflection loss −40.1 dB at 10.7 GHz and, NBC/Fe_3O_4 composites were prepared by $ZnCl_2$ activation method and *in situ* synthesis. First, nanoporous carbon was synthesized to create dielectric loss from walnut shell by a simple $ZnCl_2$ activation method and then pyrolysis process was performed. The measurement of absorption of electromagnetic waves of NBC showed the minimum reflection loss value of -36.9 dB at 8.2 GHz (Zhou et al., 2019).

Recent studies by He et al., have shown that making binary composites with carbon and $NiFe_2O_4$ is an attractive route to improve electromagnetic attenuation performance. Microwave attenuation can improved by the synergistic effect of dielectric and magnetic loss, which originates from the induction of multiple relaxation and multiple resonances. To obtain lightweight and high-efficiency adsorbents, $NiFe_2O_4$/cotton activated carbon fibers were fabricated *via* calcination and subsequent hydrothermal synthesis. The minimum value of RL has reached *via* calcination and subsequent hydrothermal synthesis. The minimum value of RL has reached −55.8 dB (Li et al., 2019). The minimum RL of $NiFe_2O_4$/carbon orepared biomass porous pomelo peel composites can reach −50.8 dB and an effective bandwidth of 4.9 GHz. The enhanced microwave absorptivity was attributed to the strong attenuation constant, unique hierarchical porous structure.

For significant absorption using an adsorbent, it is necessary to have magnetic or electric dipole protectors to be able to react with electromagnetic fields. These magnetic dipoles can protect by absorbing iron oxide. Due to their high conductivity, metal materials are the best protectors for reflecting and absorbing electromagnetic waves, but due to their high density and high corrosiveness, their use is limited (Wang et al., 2019a).

For this research, we needed a dielectric material with high absorption, larg and porous surfaces bringing vast heterogeneous interfaces desirable for polarization loss. Therefore, several biological materials were investigated for this purpose, the results of FESEM images and BET showed that oleaster seeds have good porosity and the presence of macropores and mesopores causes the trapping of incoming electromagnetic waves, boosting multiple reflections and scatterings, relaxation loss, and impedance matching.

TABLE 1 The amount of precursors and AC used.

Sample	$FeCl_3.6H_2O$ (g)	$FeCl_2.4H_2O$ (g)	NaOH (g)	AC (g)
Fe_3O_4/AC−25%	3.502	1.288	2.07	0.5
Fe_3O_4/AC−50%	2.334	0.858	1.381	1
Fe_3O_4/AC−75%	1.167	0.429	0.691	1.5

The results from the recent literature have motivated our group to architect the microwave absorbing composites of ferrites and activated carbon, obtained from Oleaster seeds. The facile and affordable synthetic approach used to prepare the nanocomposites, as well as the remarkable electromagnetic properties of the fabricated composites, present the promising prospect of tailoring high-performance microwave absorbing materials, architected by biomass-derived materials strengthened by ferrites. The goal was to prepare magnetic nanocomposite with relatively low density, superior mechanical properties, good dissipation performance, environmental benignity and non-toxicity and high electromagnetic wave absorption with 90% absorption in the X-band range and suitable bandwidth in low thickness.

2 Experimental

2.1 Materials

Iron (ll) chloride tetrahydrate ($FeCl_2.4H_2O$, 99%) and Iron (lll) chloride hexahydrate ($FeCl_3.6H_2O$, 99%) metal salts, sodium hydroxide pellets (NaOH, 99%), Zinc chloride ($ZnCl_2$, 99%) manufactured by Merck Company and hydrochloric acid (HCl, 37%) USP.

2.2 Preparation of AC

First, the Oleaster seeds were rinsed and dried. Then the dried seeds were ground to a fine powder using a high-speed grinder. Subsequently, the obtained powder was soaked in $ZnCl_2$ (2 M) for 24 h at a mass ratio of 1:1, and then the suspension was dried in an oven at 110°C for 5 h. The obtained structure waspyrolyzed in a furnace under a nitrogen environment at atemperature of 700°C for 1.5 h. Next, the obtained sample wassoaked in hydrochloric acid (HCl, 0.1 M) for 24 h, passed through a filter, washed several times with deionized water to neutral pH, and allowed to dry at 110°C (Figure 1A, B).

2.3 Preparation of Fe_3O_4/AC composites

To prepare Fe_3O_4/AC nanocomposites with mass ratios of 25, 50, and 75 wt% of activated carbon according to Table 1, a co-

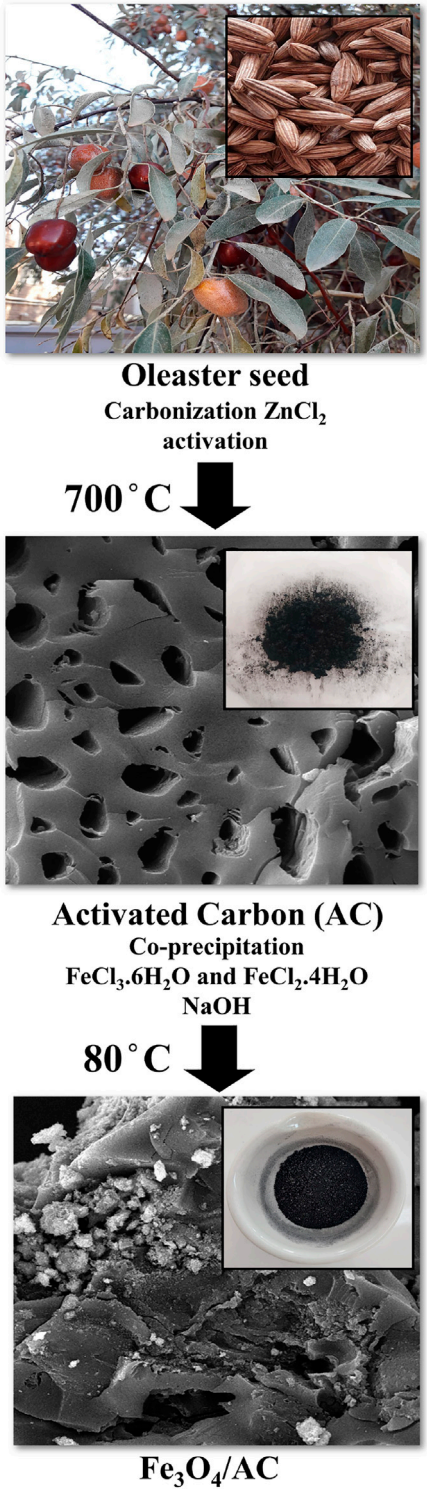

FIGURE 1
Schematic illustration of the fabrication of Fe_3O_4/Activated Carbon (AC) nanocomposites.

precipitation method was applied. Firstly, $FeCl_3.6H_2O$ and $FeCl_2.4H_2O$ salts (Merck Co.) were dissolved in deionized water in a molar ratio of 2:1 by a magnetic stirrer. Then, the solution was heated to 80°C. Afterward, the activated carbon was added and the suspension stirred for 30 min. Eventually, sodium hydroxide as a reductive agent was added to prepare Fe_3O_4/AC. The achieved slime was washed several times using deionized water. A schematic illustration of the synthetic procedure is shown in Figure 1C.

2.4 Characterization

2.4.1 XRD

TD-3700 X-ray diffraction (XRD) instrument with a wavelength of 1.54 Å and Cu-Kα radiation was employed to analyze the crystal structure of nanocomposites. The analysis accuracy of the device is 0.02° per 0.5 s, and the voltage and current used are 30 kV, respectively.

2.4.2 FTIR

The available infrared fourier transform (FT-IR) spectrometer, model TENSOR 27, made in Germany, brucker company, with a spectral range of 400–4,000 cm^{-1} and a measurement accuracy of 0.1 cm^{-1} (wave number accuracy) was used to identify chemical functional groups.

2.4.3 SEM

The morphology of the fabricated samples was investigated by MIRA3-TESCAN field emission scanning electron microscope (FESEM). The resolution of this device is up to 1 nm, and its magnification power is up to 1 million times the voltage of 30 kV. This device is equipped with an EDX (Energy-dispersive Xray Analysis) detector and can analyze samples qualitatively and quantitatively.

2.4.5 VSM

Hysteresis loops were obtained with a vibrating sample magnetometer (VSM) manufactured by MDK (Maghnatis Daghigh Kavir Co.).

2.4.6 Raman

Raman spectroscopic measurements were performed with ANDOR kymera device to characterize the graphitization of carbon with a 514 nm laser.

2.4.7 VNA

The nanocomposites were homogeneously mixed with paraffin wax by a mass ratio of 2:1 in the rectangular shape with the dimension of 22.8 × 10.16 × 2 mm to evaluate

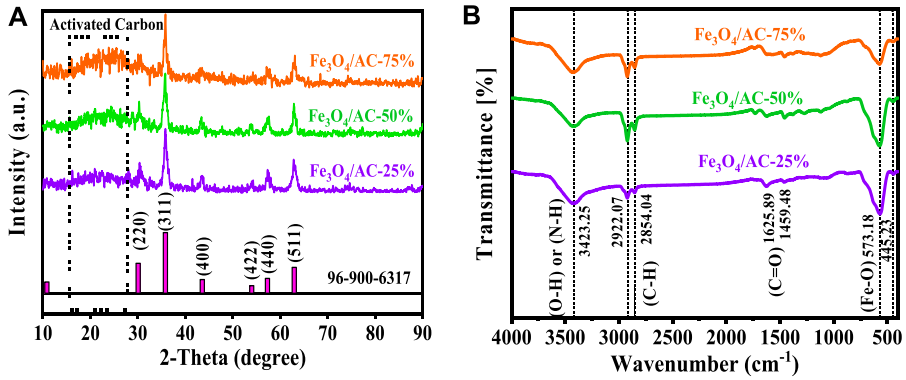

FIGURE 2
(A) XRD pattern, **(B)** FTIR spectrum of Fe_3O_4/AC nanocomposites.

microwave absorbing characteristics. The Hp8510c device is related to the measurement of network parameters, which was done by Agilent's 3.5 mm coaxial calibration kit. This set generates a frequency range of 8–12 GHz and applies it to the samples *via* wave.

3 Results and discussions

As shown in Figure 2A, the crystal structures of Fe_3O_4/AC in various mass fractions of conjugated carbon structure, including 25, 50, and 75%, were determined by XRD. The diffraction peaks indicated by 2θ at 30.37°, 35.81°, 43.59°, 54.30°, 57.60°, and 62.96° correspond to (220), (311), (400), (422), (440) and (511) lattice planes of Fe_3O_4 cubic spinel phase with the Fd3m space group (96-900-6317). Also, no additional peak was detected in the XRD patterns of Fe_3O_4/AC composites, attesting to the high purity of the products (Zong et al., 2013). A broad peak at 20–30° can be attributed to the generated amorphous phase of graphite (002), which was more clearly visible with increasing the carbon-based structure in the composite. *(α)* is the lattice constant and (V_{uc}) is the volume of the unit cell. of the nanoparticles were calculated using the following equations:

$$a = d\left(h^2 + k^2 + l^2\right)^{1/2} \quad (1)$$

$$V_{uc} = a^3 \quad (2)$$

In Eq. 1 the *d* is the spacing between planes in atomic lattice, and *h*, *k*, and *l* are Miller indices. The lattice constant (*a*) was equal to 8.31 Å, and the unit cell volume (V_{uc}) was 575.01 Å^3. The crystallite size of Fe_3O_4 was calculated by Scherrer's formula (Dong et al., 2020).

$$D = \frac{0.89\lambda}{\beta \cos\theta} \quad (3)$$

where D, λ, β, and θ are defined by the crystallite size, X-ray input wavelength, full widths at half maximum (FWHM), and Bragg angle, respectively. The average Fe_3O_4 grain size in the nanocomposites (25, 50, and 75%) was approximately 15.23, 20.4, and 16.53 nm, respectively.

The chemical functional groups of Fe_3O_4/AC samples were investigated using FTIR spectra in a range of 450-4,000 cm^{-1} and the achieved results are shown in Figure 2B. The shallow bands at 1625.89 and 1459.48 cm^{-1} are attributed to the stretching vibrations of C = C and C-C chemical species in the carbonized structure, meanwhile the broadband absorption at 3,423.25 cm^{-1} is related to the stretching vibration of hydroxyl groups. The peaks at 2,922.07 and 2,854.04 cm^{-1} are ascribed to the symmetric and asymmetric stretching vibrations of C-H existing in the unsaturated structure after the pyrolysis route. The stretching vibrations of Fe-O in octahedral and tetrahedral sites in the spinel structure were confirmed by the peaks observed at 573.18 and 445.23 cm^{-1} (Wu et al., 2015; Song et al., 2017; Gao et al., 2019; Sekar et al., 2019; Peymanfar and Moradi, 2020; Peymanfar et al., 2021b; Keykavous-Amand and Peymanfar, 2021; Peymanfar and Ghorbanian-Gezaforodi, 2021). The FTIR spectra and X-ray diffraction curves testify that the crystalline phase of spinel ferrite and conjugated carbon-based structure formed.

Raman spectroscopy was used to find vibrational modes toward finding the degree of graphitization of the samples and further study the growth of Fe_3O_4 on carbon (Figure 3A). For carbonaceous materials, two visible peaks around 1341 cm^{-1} and 1583.26 cm^{-1}, considered D and G bands, respectively (Xi et al., 2017). The graphitization degree of a composite largely determines the dielectric properties, affecting the electromagnetic wave absorbing performance in Fe_3O_4/AC. In another work done by Li et al. (2022) a simple and cost-effective structural adsorbent was proposed to significantly expand the adsorption bandwidth of biochar from banana peel (BPC). Amorphous characteristics of BPC are further confirmed by Raman spectrum and two peaks at about 1327 and 1561 cm^{-1} are attributed to D band G band, respectively, which show the amorphous characteristics of synthesized BPC.

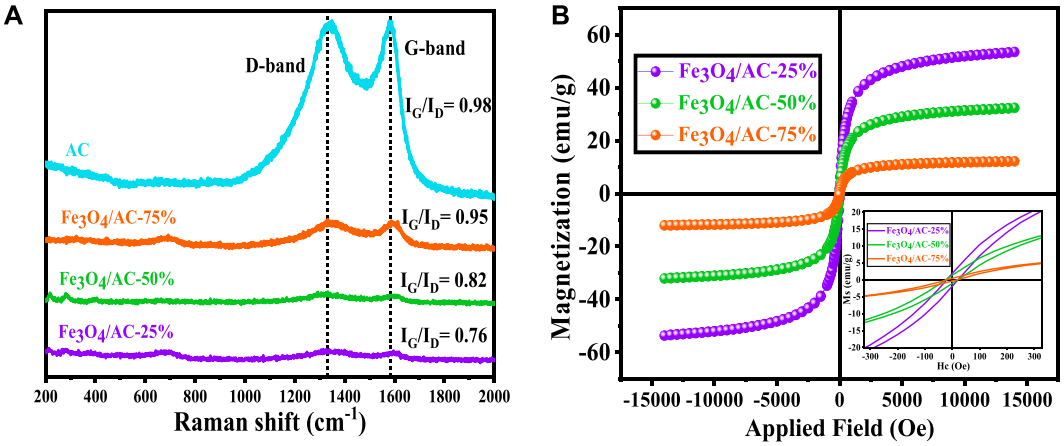

FIGURE 3
(A) Raman spectrum of activated carbon and Fe_3O_4/AC, **(B)** Magnetic hysteresis loops for Fe_3O_4/AC nanocomposites.

The G band represents the stretching vibrations of graphitic carbon, which is related to the sp^2 graphitic network-oriented bond (C = C), and the D band is pertaining to sp^3 hybridization. The position and intensity of the peaks are strongly influenced by doping and defects (Zickler et al., 2006; Wu et al., 2018). The intensity ratio of the I_G/I_D peaks depicts the graphitization ratio of the carbon materials, of which the 25%, 50%, and 75%, and activated carbon samples were 0.76, 0.82, 0.95, and 0.98, respectively. The D band is associated with the defects and distortion of the carbon atom network. In contrast, the G band is related to the regular graphitic structure of the conjugated carbon atoms (Qing et al., 2015; Yang et al., 2016). Many defects are formed after the modification of carbon with Fe_3O_4 nanoparticles. These defects act as effective polarization centers when exposed to electromagnetic waves, which can ultimately contribute to the electromagnetic wave absorption and attenuation performance of Fe_3O_4/AC composites. Also, the Raman spectrum data attest to the successful synthesis of Fe_3O_4/AC composites.

A vibrating sample magnetometer (VSM) was used to measure the magnetic properties of Fe_3O_4/AC composites at 25, 50, and 75% (Figure 3B). The S-type magnetic hysteresis (M-H) curves exhibit ferromagnetic behavior. The saturation magnetization (M_s) of 25, 50, and 75% was 53.44, 32.35, and 12.12 emu g^{-1}, respectively. M_s values of composites were reduced by enhancing the carbon content, which is mainly attributed to the presence of the non-magnetic phase. The increase of M_s improves the magnetic permeability and impedance matching of the architected composite, and as a result, microwave absorption can be promoted (Wang et al., 2020b). The values of coercivity (H_c) of 25, 50, and 75% samples are equal to 20.84, 20.24, and 17.7 (Oe), respectively, exposing that the hysteresis loops are diminished by descending the magnetic content. H_c and M_s are the crucial factors paving the way for magnetic loss.

TABLE 2 Magnetic parameters of samples measured by VSM.

Sample	M_S(emu/g)	M_R(emu/g)	H_C(Oe)	M_R/M_S
Fe_3O_4/AC–25%	53.44	1.90	20.84	0.035
Fe_3O_4/AC–50%	32.35	1.35	20.24	0.041
Fe_3O_4/AC–75%	12.12	0.47	17.17	0.038

According to Table 2, with the increase of carbon in the samples, the amount of H_c has decreased. As the particle size decrease, the domain wall disappears, and as a result, H_c increases, and when it reaches a state containing only single-magnetic dipoles, the amount of H_c decreases. Reducing the size of the particles leads to the reduction of the magnetic dipole number containing it. And, in turn, leads to a decrease in the magnetic reluctance caused by internal pair interactions between magnetons. When the particle size decreases further, the particle enters the superparamagnetic regime (Sung Lee et al., 2015).

Hysteresis loss is Cused by the magnetization and demagnetizing og the core as current flows forward and reverses directions as the magnetizing force (current) increases, the magnetic flix increases. But when the magnetizing force (current) is decreased, the magnetic flux doesn't decrease at the same rate, but less gradually. Therefore, when the magnetizing force reaches zero, the magnetizing force must be applied in the negative direction, the relationship between the magnetizing force, H, and the flux density, B, is shown on a hysteresis curve, or loop. The area of the hysteresis loop shows the energy required to complete an entire cycle of magnetizing and demagnetizing, and the area of the loop represents the energy lost during process.

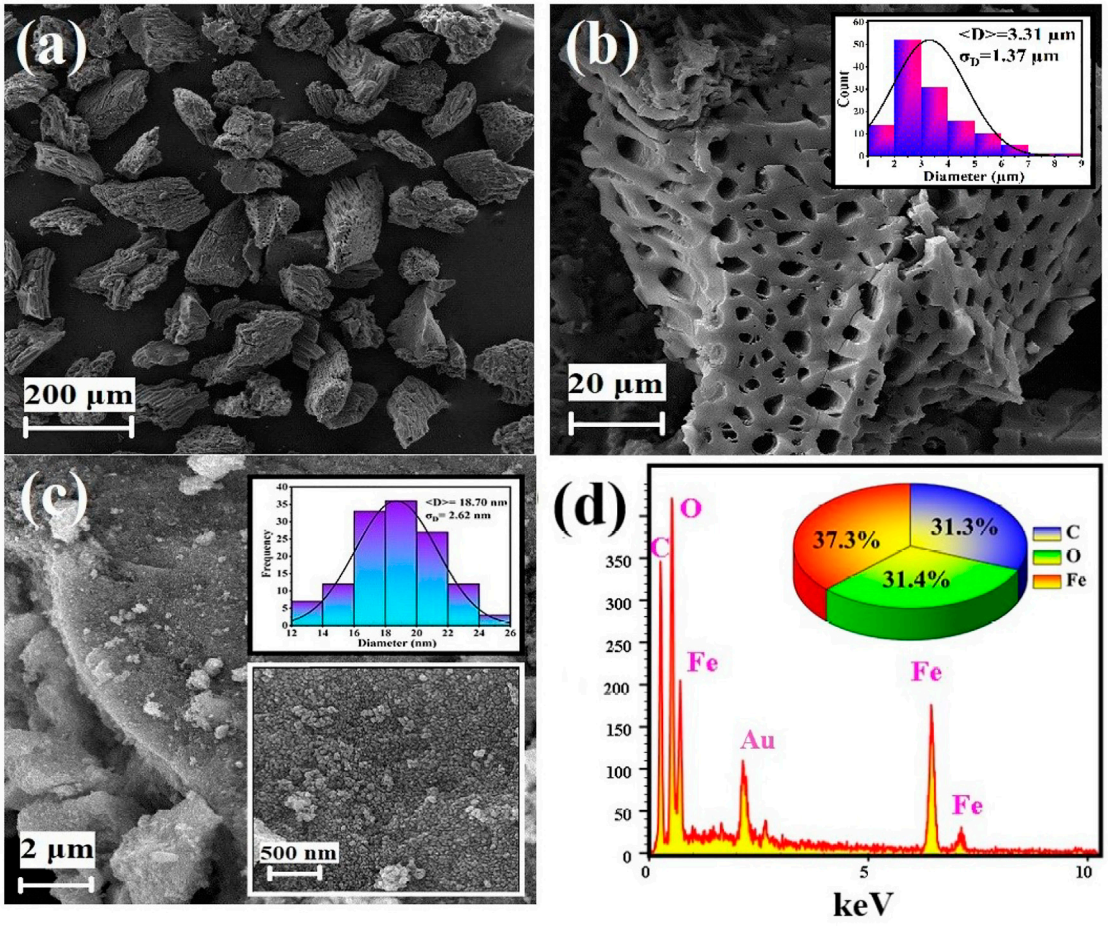

FIGURE 4
(A) and **(B)** FESEM images of Olestear seeds drived activated carbon (AC), and **(C)** FESEM image of Fe_3O_4/AC nanocomposite. **(D)** EDX spectra of Fe_3O_4/AC sample.

The morphology of the samples was examined using FESEM micrographs (Figure 4). It is noteworthy that the biomass-derived material activated by $ZnCl_2$ has many tiny pores (Figure 4A,B). Additionally, in the 25% sample, Fe_3O_4 nanoparticles are extensively dispersed on the porous carbon surface (Figure 4C), compared to the 75% and 50% samples, due to the increase in $FeCl_2.4H_2O$ and $FeCl_3.6H_2O$ precursors, bringing the more magnetic Fe_3O_4. As mentioned, in sample Fe_3O_4/AC-25%, due to more precursprs, Fe_3O_4 nanoparticles are homogeneously placed on the carbon matrix and hole. Abundant pores in the carbonized structure realize multiple reflections and scattering of incident waves, attenuating microwave, and eventually converting them into thermal energy. It can be seen that the size of magnetic particles in 25, 50, and 75% samples are 18.70, 23.69, and 29.36 nm, respectively. The pore size of pure carbon belongs to the micron level. Also, the average pore size is approximately 3.31 µm.

As can be seen from the EDX analysis (Figure 4D), the uniform dispersion of oxygen, iron, and carbon elements are confirming that the Fe_3O_4 particles are evenly anchored throughout the composite. In order to prepare the samples, conductive materials such as gold are used with 10 nm layer deposition, which is the reason for the presence of the gold peak.

The BET diagram, also called the isothermal adsorption and desorption diagram, is a linear diagram from which the effective surface area of the substance is extracted. After the cell containing the desired sample is placed in the liquid nitrogen tank, the amount of gas absorbed by the substance is calculated by gradually increasing the nitrogen gas pressure in each step. Then, with the gradual reduction of the gas pressure, its desorption rate is measured. Finally, the graph of the volume of nitrogen gas adsorbed and desorbed by the substance is drawn based on the relative pressure at a constant temperature. Nitrogen adsorption experiments were conducted to further

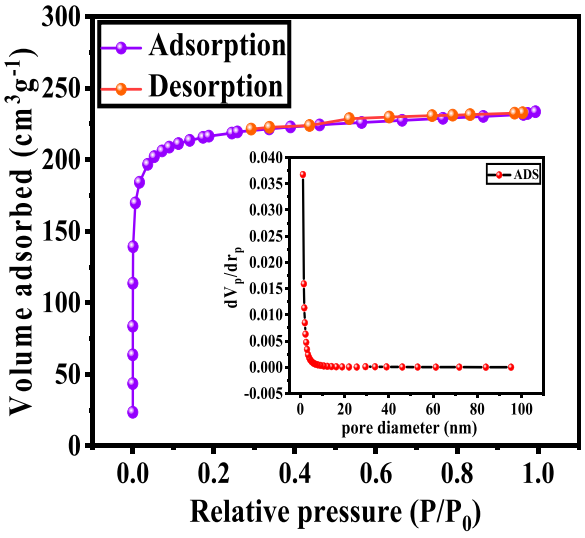

FIGURE 5
N_2 adsorption/desorption isotherm and pore size distribution of activated carbon.

study the pore size and surface area of AC. This analysis presents the holes size distribution based on their radius, which is the most frequent (1.21 nm was used) (Yan et al., 2019). The total volume of the cavities was 0.0473 $cm^3 g^{-1}$, and the specific surface area was 60.157 $m^2 g^{-1}$. Figure 5 exhibits that pyrolyzed biomass has the overall type IV isotherm, which corresponds to the mesoporous structure. Moreover, the pore distribution curves are shown in Figure 5. Evidently, the activated carbon has high pores and surface area, benefiting the microwave absorbing performance by elevating the polarization loss as well as multiple reflections and scattering.

The VNA device is related to the measurement of network parameters, which was done by Agilent's 3.5 mm coaxial calibration kit. This set generates a frequency range 8–12 GHz and applies it to the samples *via* wave. This device is connected to the waveguide with two coaxial cables through port 1 and port 2, and then it is set to the corresponding frequency and sends the wave. Two sensore are installed at both ends of the wave and record the amount of sent and received waves. The absorption value of the sample is obtained from the difference between the incident and transmitted waves. The performance of this set is such that we must calibrate this device before any test. In the first step, we calibrate the device with three methods of mathematical loading, open loading and short loading. Mathematical loading calibration using the short loading method on the device. In the next step, we have to perform the relevant calibration using the short loading method on the device. In this case, without placing the waveguide, we connect the two ends connected to the waveguide and perform the corresponding calibration by generating a wave by the device. In the final stage of calibration or open loading, we keep one end of the waveguide open and perform the corresponding calibration on it. After performing the initial calibration steps, once without placing the samples in the waveguide, we apply the frequency of the X band it and save its absorption graph as numbers and a reference graph for comparison with the original samples. Then we place the original samples one after the other in the waveguide and take their absorption as a function of frequency and store the relevant information.

The relative complex permittivity ($\varepsilon_r = \varepsilon' - j\varepsilon''$) and magnetic permeability ($\mu_r = \mu' - j\mu''$) are two main factors affecting the microwave absorbing capability (Hou et al., 2020). The real parts show the ability to store electromagnetic energy and examine the polarization and magnetization of matter under the influence of an electromagnetic field. And the imaginary parts represent the electric and magnetic energy losses (Qi et al., 2016; Wang et al., 2016). As shown in Figures 6A–D, in this research, the electromagnetic parameters of nanocomposites were measured in the range of 8–12 GHz. When iron ferrite is combined with activated carbon to form Fe_3O_4/AC composites, ε' and ε'' increase with increasing conjugated carbon-based content. Therefore, magnetic losses originating from Fe_3O_4 nanoparticles, and dielectric losses generated from activated carbon, together improve the microwave absorption performance. Strong potential to store and dissipate electrical energy, and proper impedance matching, play a vital role in microwave attenuations (Li et al., 2018b). According to the free electron theory, where σ is the conductivity, ε_0 is the permeability of free space. It can be seen from the equation $\varepsilon'' = \sigma/(2\pi\varepsilon_0 f)$ that a large value og induces a high value of ε'', which indicates that Fe_3O_4 decorated Carbon exhibits better conductivity performance. In Fe_3O_4 crystal structures, Fe^{2+} and Fe^{3+} ions show a random distribution in their octahedral position and electrons can be rapidly transferred between the two valence states of iron ions to achieve excellent conductivity. As shown in the figure, the values of ε' and μ' of the composites show a slight decreasing trend with increasing frequency from 8 to 12 GHz, such a phenomenon may occur in many carbon nanomaterials, which is called frequency dispersion behavior. Carbon is useful for forming conductive paths. The ε and μ values of the sample show oscillation, and the resonance peak appears in the frequency range because more holes and defects (Yan et al., 2022). Optimal impedance matching occurs where the relative complex permittivity and permeability are close enough and have an appropriate paradigm. The dielectric loss tangent ($\tan\delta_\varepsilon = \varepsilon''/\varepsilon'$) and magnetic loss tangent ($\tan\delta_\mu = \mu''/\mu'$) are shown in Figure 6E,F. The contribution of dielectric and magnetic losses in the total microwave absorbing performance is determined by comparing the loss tangent values (Wang et al., 2018). It can be seen that δ_ε values of the samples are more prominent than δ_μ values in the frequency range of 8–12 GHz. This phenomenon suggests that the dielectric loss has a more significant effect than the magnetic loss in the samples.

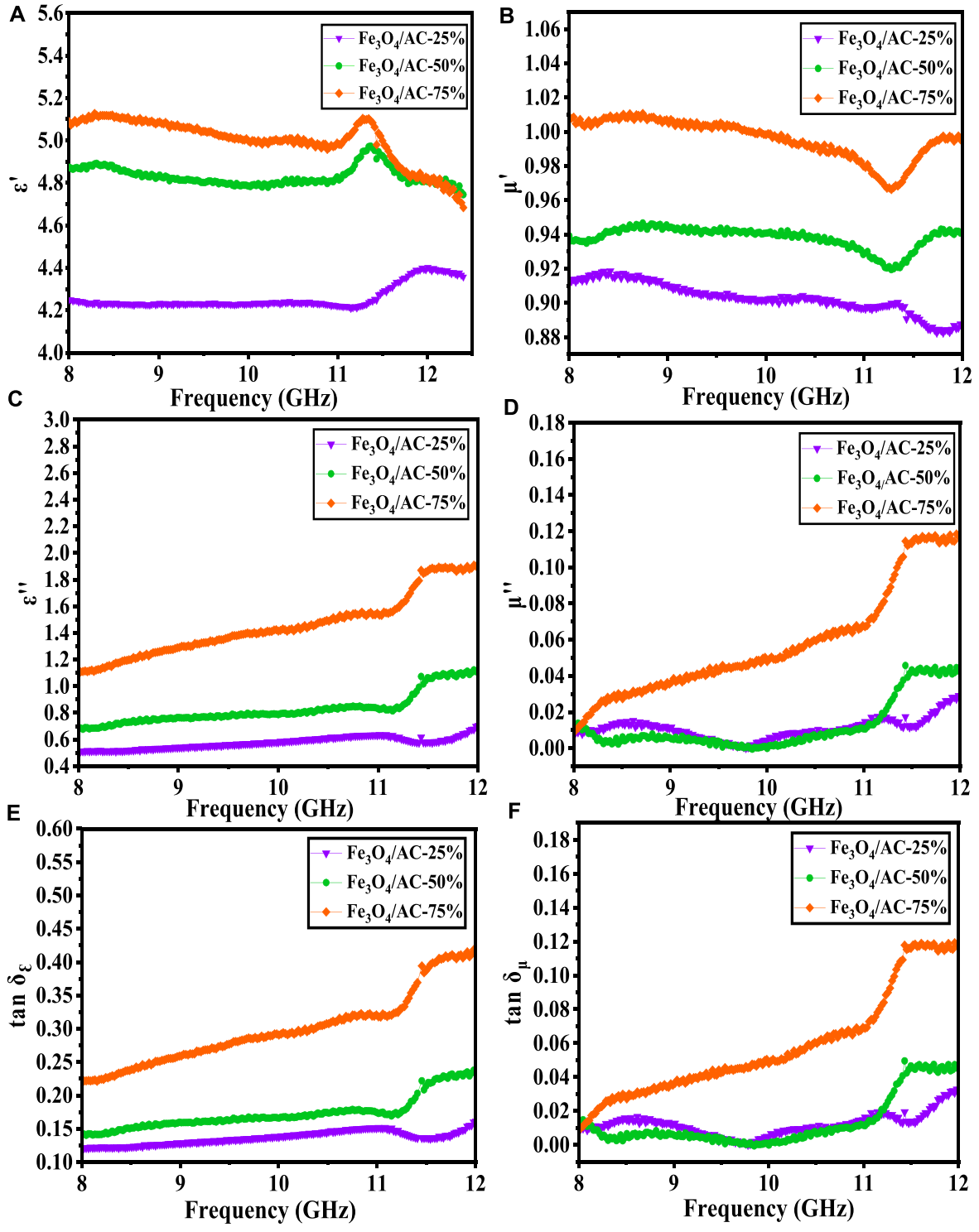

FIGURE 6
(A) Real part, and **(B)** Imaginary part of complex permittivity. **(C)** Real part, and **(D)** Imaginary part of complex permeability. **(E)** The dielectric loss tangent and **(F)** The magnetic loss tangent of the samples.

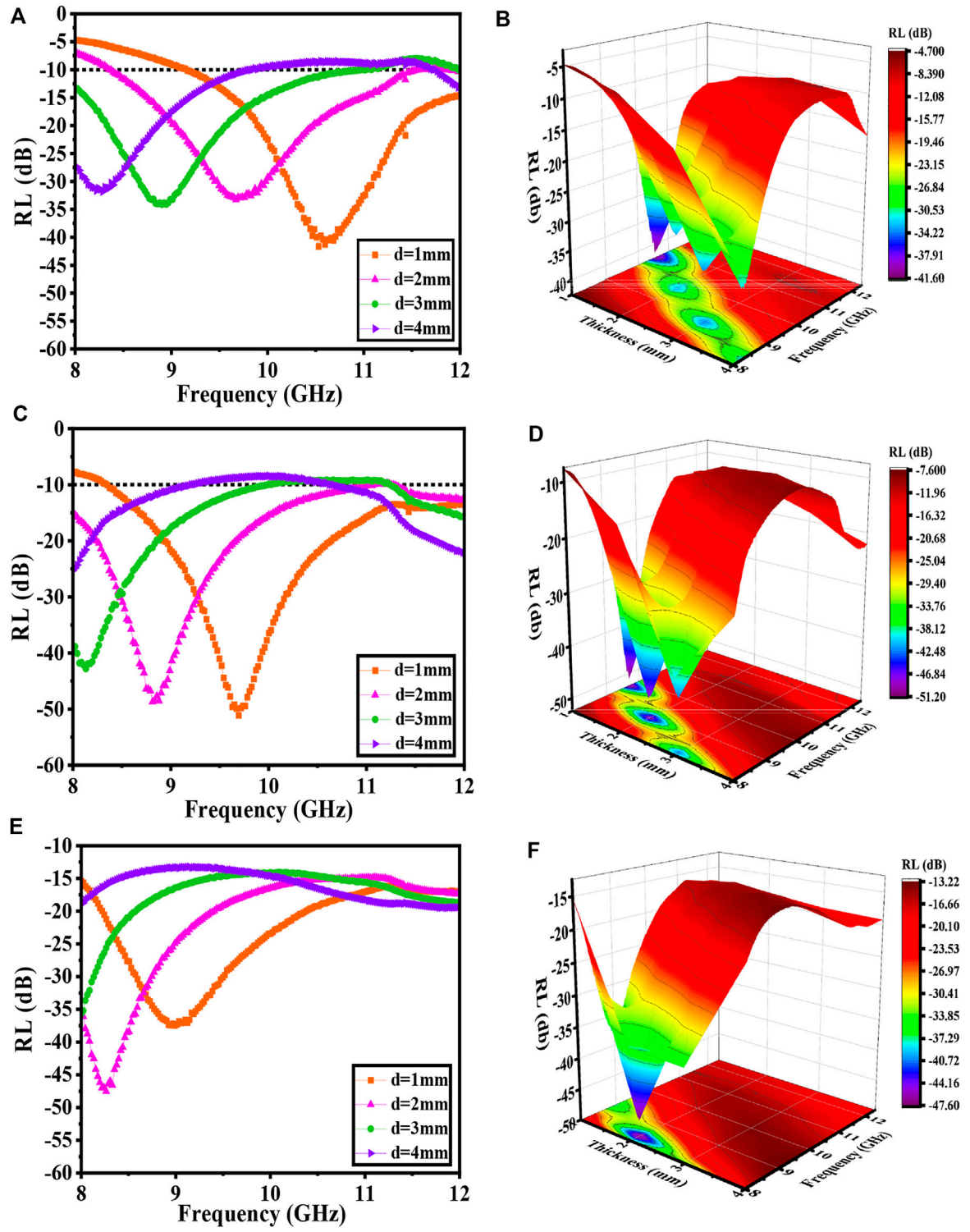

FIGURE 7
Frequency-dependent RL curves and three-dimensional contour maps of AC-25% **(A)** and **(B)**, AC-50% **(C,D)**, and AC-75% **(E,F)**.

Based on the transmission line theory, the reflection and transmission of an incident wave from the interface of absorbing materials can be expressed by the reflection coefficient and the transmission coefficient, respectively, which are all related to the input impedance (Z_{in}) (Ding et al., 2016; Yang et al., 2018; Yu et al., 2018).

TABLE 3 The results of reflection loss in different thickness.

Samples	Fe_3O_4/AC-25%				Fe_3O_4/AC-50%				Fe_3O_4/AC-75%			
d (mm)	1	2	3	4	1	2	3	4	1	2	3	4
F (GHz)	10.25	9.67	8.89	8.23	9.69	8.83	8.13	—	8.97	8.25	—	—
RL (dB)	−41	−33	−34	−32	−51	−48	−43	—	−37	−47	—	—
Bandwidth (GHz)	—	3.22	—	—	—	—	—	—	—	—	—	—

$$Z_{in} = Z_0\sqrt{\frac{\mu_r}{\varepsilon_r}}\tanh\left(j\frac{2\pi fd}{c}\sqrt{\mu_r\varepsilon_r}\right) \quad (4)$$

Z_0, f, c, and d are defined as the characteristic impedance of the free space, microwave frequency, wave speed in the free space, and thickness of the absorbing material, respectively. RL is expressed based on electromagnetic parameters through transmission line theory (Li et al., 2018b).

$$RL = 20\log\left|\frac{Z_{in} - Z_0}{Z_{in} + Z_0}\right| \quad (5)$$

An ideal microwave absorbing material must not only have strong absorption but also have characteristics such as low thickness and wide efficient bandwidth. When the RL value is below -10 dB, it represents that more than 90% of incident electromagnetic wave energy is absorbed. Generally, the sum of the frequencies where RL values are below 10 dB can be considered an efficient bandwidth.

The efficient absorption bandwidth can be obtained in the range of 8-12 GHz with diverse matching thicknesses. The maximum absorption value of the 25% sample shows -41.45 dB at 10.59 GHz when the thickness is 1 mm (Figure 7A,B) but when the matching thickness is 2 mm, its maximum RL value is −33.29 dB at 9.67 GHz, and the efficient absorption bandwidth is only 3.22 GHz. When the matching thickness becomes thicker and reaches 3 mm, the maximum RL value is −34.25 dB at 8.89 GHz. In this way, it can be concluded that the matching thickness has an essential effect on the microwave absorbing performance. For Figure 7C,D and the 50% sample, the RL value is equal to −51.22 dB in the thickness of 1 mm at the frequency of 9.69 GHz, the RL value is equal to −48 dB in the thickness of 2 mm at the frequency of 8.83 GHz, and in the thickness of 3 mm, the value of RL is −42.99 dB at the frequency of 8.13. The RL value at the frequency of 8.97 GHz with a thickness of 1 mm is −37.63 for the 75% sample. Meanwhile, for the thickness of 2 mm, the absorption value is −47.84 at the frequency of 8.25 GHz (Figure 7E,F). Noticeably, the 25% sample illustrated the maximum absorption value of −33.29 dB at 9.67 GHz and the efficient absorption bandwidth of 3.22 GHz with 2 mm in thickness (Table 3). Its performance is significantly better than other samples because the excellent electromagnetic absorption performance is supplied with a thin absorber thickness. Furthermore, carbon-based microwave absorbing materials are listed and compared in Table 4. The electromagnetic wave absorption significantly deteriorates where too much-conjugated carbon structure is introduced into the composites, originating from the amplified impedance mismatching. Notably, the prepared samples show a broad efficient bandwidth along the X-band at a thin thickness. In another study by Wu et al. (2022) biomass-derived carbon (BHPC) with micropores, mesopores, and macropores obtained from rice husk was prepared using KOH activation and one-step carbonization. When the thickness is 2.8 mm, the BHPC samples obtained at 650°C show excellent electromagnetic absorption properties with a minimum reflection loss of −47.46 dB at 9.80 GHz and an effective absorption bandwidth of 81% of it forms the X-band (8.47–11.87 GHz). It exhibits good absorption performance for electromagnetic waves due to good impedance matching, high dielectric loss capacity, larg specific surface erea, aand reasonable pore diameter distribution. This study shows that porous carbon from rice husk has a wide prospect as a lightweight and efficient electromagnetic absorber material (Wu et al., 2022).

Generally, matching the relative impedance $|Z_{in}/Z_0|$ is an important factor affecting the microwave absorbing performance. In an ideal case, the electromagnetic wave can enter the material completely without any reflection, and the Z value is equal to 1. As shown in Figures 8A–F, the relative impedance matchings $|Z_{in}/Z_0|$ states that the 25% and 50% samples compared to the 75% sample are closer to 1. In another work by Wang et al. (2019b) Fe_3O_4/PJBC composites were successfully prepared by chemical deposition method at 60°C. Jute was used as the carbon source because it is low cost and easy to fabricate the porous carbon matrix. After coating with Fe_3O_4 particles, the impedance matching of the composites is improved and the microwave absorption performance of Fe_3O_4/PJBC composites is greatly improved compared to Fe_3O_4 magnetic particles. In addition, many interfaces, Ion polarization, eddy loss, natural resonance, and multiple reflection and scattering play an important role in improving the absorption performance of electromagnetic waves. In this way, the attenuation constant can be used to describe the attenuation capacity of the absorbers. Moreover, when the thickness of the absorber increases, the peak moves to lower frequencies, represented by the quarter wavelength mechanism. As given by the following equation, the more attenuating

TABLE 4 Electromagnetic absorption performance of recently reported magnetic/carbon-based absorbers.

Sample	RL (dB)	Absorption bandwidth (GHz)	Thickness (mm)	Ref
Fe_3O_4@C (Walnut shell)	−56.61	2.72	2.46	Li et al. (2020)
Porous Carbon/$CoFe_2O_4$ derived from Eggshell	−49	4.1	1.5	Jain et al. (2016)
Rice husk-based porous carbon/Fe	−40.1	2.7	1.8	Fang et al. (2017)
Dopamine/Fe_3O_4	−50.8	3.5	1.5	Guo et al. (2019b)
Wheat straw/Fe_3O_4/Fe	−33.6	3.3	4.7	Gou et al. (2019)
Fe_3O_4/RGO composites	−44.6	4.3	3.9	Huang et al. (2016)
Fe_3O_4/AC (Oleaster seeds)	−51.12	~4	1	This work

potential leads to a thinner matching thickness (Zhang et al., 2015b; Peymanfar and Ghorbanian-Gezaforodi, 2020; Peymanfar et al., 2021c).

$$t_m = \frac{nc}{4f_m\sqrt{|\mu_r\varepsilon_r|}} \tag{6}$$

where, f_m and t_m represent the matching frequency and thickness, respectively. It can be seen from Figures 7, 8 that the peak position of all samples changes from higher frequencies to lower frequencies by increasing the thickness. In other words, the matching thickness (t_m) and matching frequency (f_m) satisfy Eq. 6 for all samples. This phenomenon is associated with the canceling of the propagated waves from the interface checkpoint of the absorber by the reflected waves from the metal plate that the microwave absorber is laid on its surface where the incident and the reflected waves are 180° out of phase.

The electromagnetic wave absorption capability of the samples was investigated by plotting the semicircular curves of ε' *versus* ε'' (Cole-Cole semicircular) as follows (see Figures 9A–C) (Li et al., 2017).

$$\left(\varepsilon' - \frac{\varepsilon_s + \varepsilon_\infty}{2}\right)^2 + (\varepsilon'')^2 = \left(\frac{\varepsilon_s - \varepsilon_\infty}{2}\right)^2 \tag{7}$$

In the above equation, ε_s and ε_∞ represent the static permittivity and relative dielectric constant at high frequency, respectively. Each established single semicircle in the ε' vs ε'' plot attests to a Debye relaxation behavior. The defects in the tailored conjugated structures and magnetic Fe_3O_4, remained hetero atoms and functional groups in the pyrolyzed biomass, and developed heterogeneous interfaces in the nanocomposite, and absorbing media are the pivotal factors bringing relaxation loss mechanisms.

Magnetic losses in microwave regions are caused by domain wall resonance, magnetic hysteresis loss, natural resonance, eddy's current effect, and exchange resonance. Domain wall resonance is excluded in this research since this mechanism often occurs at MHz. Eddy current loss can be determined as follows (8) (Luo et al., 2015).

$$C_0 = \mu''\mu'^{-2}f^{-1} = 2\pi\mu_0\sigma\frac{d^2}{3} \tag{8}$$

Where μ_0, d, and σ are vacuum permeability, particle diameter, and conductivity, respectively. The value of $\mu''\mu'^{-2}f^{-1}$ should be constant with changing frequency if eddy current loss is the only reason behind the magnetic loss. It is well known that the skin effect occurs in conductors (Bateer et al., 2015; Datt et al., 2018). As revealed in Figure 10A, the permeability of the nanocomposites is essentially generated from the natural resonance. According to Eq. 8, conductive loss or conduction loss is caused by the fact that when electromagnetic wave propagates in absorbers, their energy will be converted into electric current. During the transmission of electric current along electromagnetic wave absorbers, their instinct resistance will generate joile heat and thus consume electromagnetic wave energy. Conductive loss exists in absorbers with high conductivity such as carbon materials. However, over high conductivity should be avoided since it undoubtedly will result in mismatch of impedance and poor electromagnetic wave dissipation capacity.

As stated, the primary source of magnetic losses is the natural resonance resulting from the effect of geometric configuration, and exchange resonance caused by ferromagnetic materials. To compare the dissipating performance of the samples, the attenuation constant (α) is obtained from the following equation (Peymanfar et al., 2020; Shamsaddin Saeed et al., 2020).

$$\alpha = \frac{\sqrt{2}\pi f}{c}\sqrt{(\mu''\varepsilon'' - \mu'\varepsilon') + \sqrt{(\mu''\varepsilon'' - \mu'\varepsilon')^2 + (\mu'\varepsilon'' + \mu''\varepsilon')^2}} \tag{9}$$

As shown in Figure 10B, by increasing the frequency, an upward trend is observed, for the 25% sample from 83.48 to 133.11, and 50% sample from 135.84 to 218.78, and 75% sample from 192.11 to 309.14. As shown, at high frequencies, both samples (50 and 75%) indicate strong attenuation ability coming from their high dielectric loss. In addition, the increase in magnetic content has caused a drop in an attenuation constant, which proves the downward

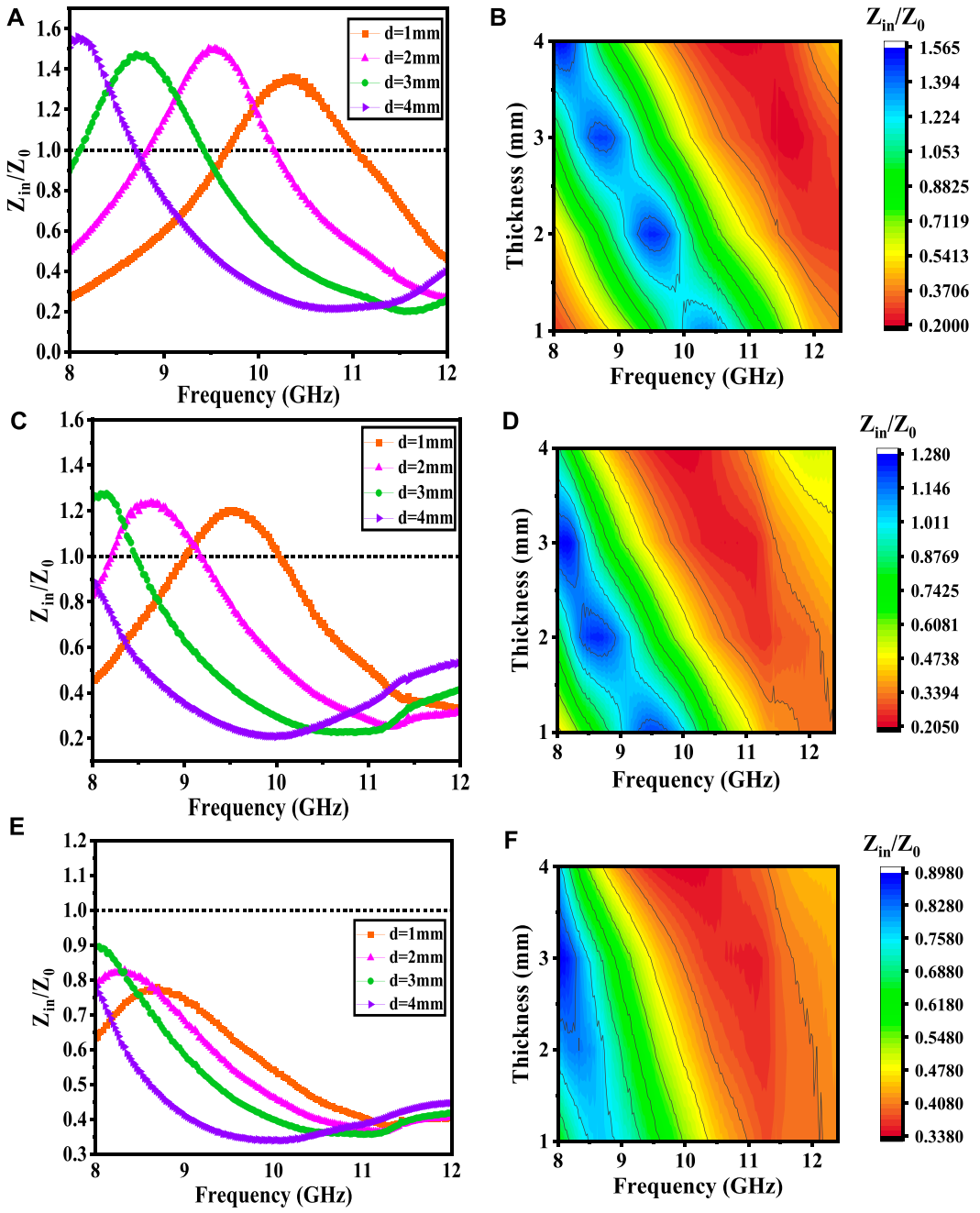

FIGURE 8
Impedance matching for Fe_3O_4/AC nanocomposites, two dimensional mapping plots of calculated Z_{in}/Z_0 values of Fe_3O_4/AC in three differentpercentages of carbon **(A, B)** AC-25%, **(C, D)** AC-50%, and **(E, F)** AC-75%.

permeability trend. Amorphous carbon with high conductivity can form a conductive network in Fe_3O_4/AC composites, which improves the electrical conductivity of the composites. However, if the complex permittivity is much higher than the complex permeability, most of the incident electromagnetic wave will be reflected from the surface of the material because it has a high surface resistance, which leads to strong reflection and weak absorption ability of electromagnetic waves. Therefore, the impedance matching of the material is weakend.

In Liu et al.'s work, α values of $CoFe_2O_4$/RGO-180, $CoFe_2O_4$/RGO-200, and $CoFe_2O_4$/RGO-220 increase from 11.4, 20.8, and 35.9 to 93.6, 230.6, and 280.4, respectively, in the frequency range

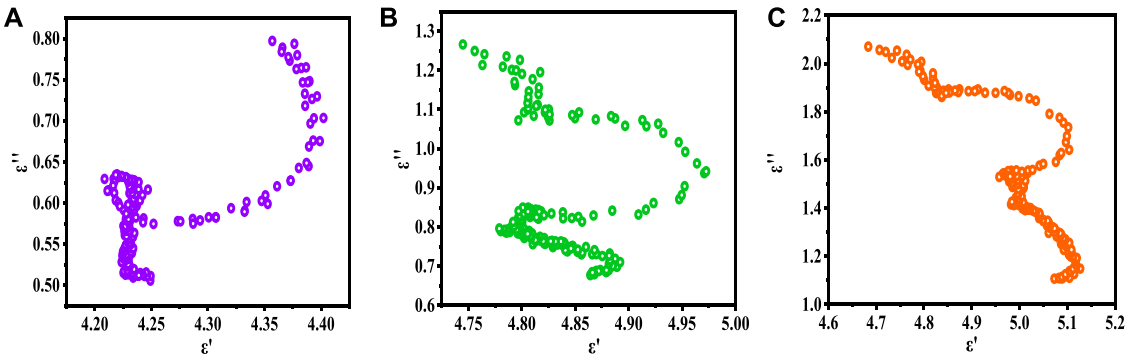

FIGURE 9
Cole-Cole semicircles of Fe_3O_4/AC nanocompositesin three different percentages of carbon **(A)** AC-25%, **(B)** AC-50%, and **(C)** AC-75%.

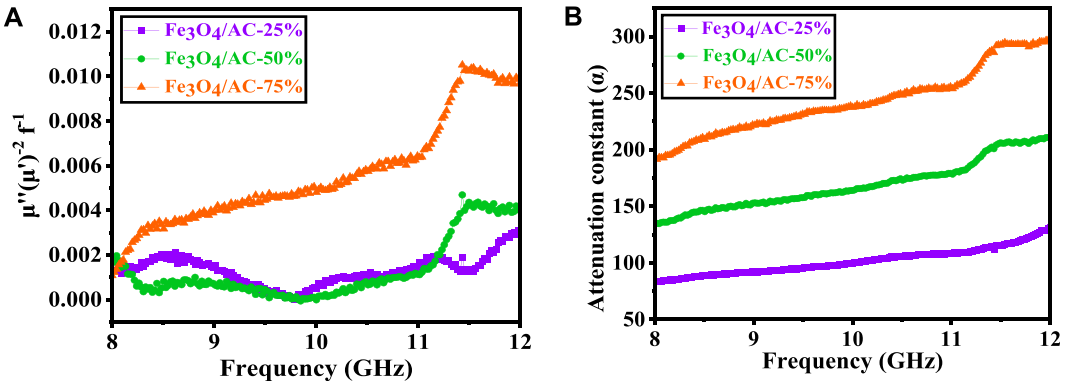

FIGURE 10
(A) C_0-f curves, **(B)** attenuation constant of all samples.

of 2-18 GHz. Typically, in the high frequency region, α values exceed 200 of $CoFe_2O_4$/RGO-200 and $CoFe_2O_4$/RGO-220 show their strong attenuation ability, which is caused by the high conduction loss and dielectric loss of RGO sheets (Liu et al., 2022).

The main loss mechanisms of electromagnetic waves for dielectric loss materials are surface polarization, dipole polarization, defect polarization and conductive loss. The effect of surface polarization has been widely used to increase the dielectric loss capacity, thereboy increasing the electromagnetic wave loss. Meanwhile, the surface polarization effect includes two interface, homogeneous or heterogeneous interfaces. The work function of homogeneous or heterogeneous interfaces is to induce surface polarization. Diverse work function can lead the carrier accumulation (carriers flow from lower to higher conductance) and subsequently polarization and relaxation process under changing electromagnetic field. Dipole or dipole polarization refers to the movement of dipoles in polar or non-polar molecules. Which is caused by the high electronegativity of oxygen ions compared to hydrogen ions, thus leading to theaccumulation of electrons around oxygen ions and the uneven distribution of the electron cloud in the water molecule. Therefore, these polar molecules act as electric dipoles and go through the process of polaeization and dipole relaxation under the change of electromagnetic field and consume its energy. In general, the loss of dipole polarization in adsorbents is caused by the presence of polar molecules and polar functional groups. Therefore, functional groups in carbon materials are the main source of dipole polarization in most researches. C-O, C-OH and C=O groups are common functional groups in electromagnetic wave absorbers. Defect sites in absorbers can trap charge carriers and break the balance of charge distribution, thus leading to the polarization process and corresponding electromagnetic energy loss. Typically, defect sites in materials can be classified into 0D point defect (such as vacancy and dopant impurities), 1D line defect (such as

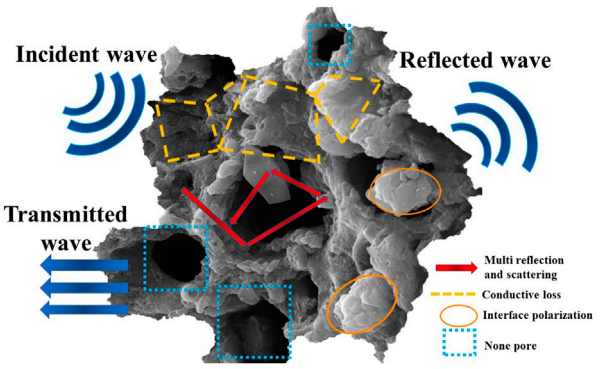

FIGURE 11
Schematic illustration of microwave absorption mechanisms of Fe_3O_4/AC nanocomposites.

edge dislocation and screw dislocation), and 2D planar defect (grain boundaries and twist boundaries). For electromagnetic wave absorbers, the common defect sites engineering is 0D point defect including oxygen vacancy regulation and heteroatoms doping. For oxygen vacancy, it is a pervasive vacancy in oxygen-contained materials owing to low formation energy. Due to the absence og oxygen atoms in lattice point, charge carriers generated under external alternating electromagnetic field will be trapped bu oxygen vacancies, leading to the accumulation og negative carriers and following polarization (Qin et al., 2022).

The remained hetero atoms, surface defects, and functional groups operate as dipole polarization centers to absorb the free space charge, leading to the relaxation loss, and converting the electromagnetic energy. Moreover, the vast heterogeneous interface in the magnetodielectric composites develops the multiple reflections and scattering desirable for the canceled waves and microwave attenuation (Cui et al., 2013; Zhao et al., 2020). Furthermore, the various heterogeneous interfaces established by the dielectric and magnetic components as well as the absorbing matrix, tune the interfacial polarization (Lei et al., 2020). In addition, the increase in polarization loss is caused by the hierarchical porous structure of pyrolyzed biomass with meso/macropores promoting the dielectric loss, eventually benefiting microwave absorption (Chen et al., 2020). The increase of ε' is caused by the polarization loss resulted from the charge accumulation, and the increase in ε'' values may be due to the improvement of relaxation and conductive loss.

Figure 11 summarizes the mechanism of microwave absorption commanding in the samples. The considerable factors satisfying the observed microwave absorbing properties of the samples are listed: the regulated impedance matching by anchoring the dielectric phase using the magnetic structure. The porous structure of the conjugated carbon-based material improved the dielectric permittivity and impedance matching so that the electromagnetic waves can more enter the composite and then be absorbed as much as possible by scattering and multiple reflections through the hierarchical porous structure. In general, polarization effects can be specific to interfacial polarization, dipole polarization, ionic polarization, and electron polarization. However, electron and ionic polarizations usually occur at higher frequency regions, meaning that the main polarization behaviors at 8–12 GHz are attributed to interfacial polarization and dipoles. Magnetic loss is another critical mechanism of microwave attenuation, which can be divided into exchange resonances, eddy current losses, natural ferromagnetic resonances, domain wall resonance, and magnetic hysteresis. Among these effects, hysteresis loss and domain wall amplification can be neglected in the 8–12 GHz waveband. By decorating the Fe_3O_4 nanoparticles on the pyrolyzed bioinspired material, more interfaces can be induced, causing more polarization loss mechanisms. In addition, the synergistic effects of macropores, mesopores, and micropores contribute to absorbing performance by augmenting the relaxation loss mechanisms. Macropores in the carbonized structure establish a proper path for the conductive networks and micro currents enhancing conductive loss. Mesopores increase the specific surface area of the material and form many solid-space interfaces, promoting interfacial polarization. The defects, as well as remaining functional groups and hetero atoms, act as polarization centers, causing dipole polarization. The carbon-based structure obtained from oleaster seeds can be used as a promising microwave absorbing material in the X-band.

4 Conclusion

A simultaneous pyrolysis scenario and chemical co-precipitation method was used to prepare Fe_3O_4/AC composites, demonstrating the salient microwave absorbing characteristics. The biomass-derived material was decorated by ferrite nanoparticles to improve microwave absorbing features. The Fe_3O_4/AC composites illustrated the excellent microwave absorption performance in X-bandwidth. The maximum RL value of −51 dB and the efficient absorption bandwidth of almost whole X-band were obtained when the thickness was only 1 mm. Additionally, the efficient absorption bandwidth can be regulated by adjusting the thickness from 1 mm to 4 mm in the X-band range. The optimal value with a bandwidth of 3.22 and absorption rate of −33 dB corresponds to sample Fe_3O_4/AC-25% with a thickness of 1 mm at frequency of 9.67 GHz, because it contains a eide bandwidth in the X-band range. Porous structure, large interfaces, defects, remaining hetero atoms, and synergistic effect between magnetic and dielectric loss of Fe_3O_4 and AC are the main factors paving the way for microwave absorption. These results also show that the porous biomass-derived structure obtained from Oleastar seeds can be a promising microwave absorber to architect novel composites. The eye-catching microwave absorbing

performance, thin thickness, free and available source, and facile experimental procedure have enhanced the importance of the presented research.

Data availability statement

The original contributions presented in the study are included in the article/Supplementary Material, further inquiries can be directed to the corresponding author.

Author contributions

MM: Original draft, formal analysis, investigation BA: Project administration, supervision, writing—review and editing RP: Analysis, advising, writing—review and editing HN: Methodology.

Conflict of interest

Author RP was empolyed by the Peykareh Enterprise Development Co.

The remaining authors declare that the research was conducted in the absence of any commercial or financial relationships that could be construed as a potential conflict of interest.

Publisher's note

All claims expressed in this article are solely those of the authors and do not necessarily represent those of their affiliated organizations, or those of the publisher, the editors and the reviewers. Any product that may be evaluated in this article, or claim that may be made by its manufacturer, is not guaranteed or endorsed by the publisher.

References

Bateer, B., Wang, L., Zhao, L., Yu, P., Tian, C., Pan, K., et al. (2015). A novel Fe_3C/graphitic carbon composite with electromagnetic wave absorption properties in the C-band. *RSC Adv.* 5 (74), 60135–60140. doi:10.1039/c5ra08623j

Chen, W., Peng, K., Wang, J., He, X., Su, Y., Zhang, B., et al. (2020). Enhanced microwave absorption properties of nickel-coated carbon fiber/glass fiber hybrid epoxy composites-towards an industrial reality. *Mat. Res. Express* 6 (12), 126324. doi:10.1088/2053-1591/ab62ee

Chen, X., Wang, Z., Zhou, M., Zhao, Y., Tang, S., and Ji, G. (2023). Multilevel structure carbon aerogels with 99.999% electromagnetic wave absorptivity at 1.8 mm and efficient thermal stealth. *Chem. Eng. J.* 452, 139110. doi:10.1016/j.cej.2022.139110

Cui, K., Cheng, Y., Dai, J., and Liu, J. (2013). Synthesis, characterization and microwave absorption properties of $La_{0.6}Sr_{0.4}MnO_3$/polyaniline composite. *Mater. Chem. Phys.* 138 (2), 810–816. doi:10.1016/j.matchemphys.2012.12.064

Datt, G., Kotabage, C., Datar, S., and Abhyankar, A. C. (2018). Correlation between the magnetic-microstructure and microwave mitigation ability of $MxCo_{(1-x)}Fe_2O_4$ based ferrite–carbon black/PVA composites. *Phys. Chem. Chem. Phys.* 20 (41), 26431–26442. doi:10.1039/c8cp05235b

Ding, Y., Zhang, L., Liao, Q., Zhang, G., Liu, S., and Zhang, Y. (2016). Electromagnetic wave absorption in reduced graphene oxide functionalized with Fe_3O_4/Fe nanorings. *Nano Res.* 9 (7), 2018–2025. doi:10.1007/s12274-016-1092-z

Dong, J., Zhang, L., Dai, X., and Ding, F. (2020). The epitaxy of 2D materials growth. *Nat. Commun.* 11 (1), 5862. doi:10.1038/s41467-020-19752-3

Fang, J., Shang, Y., Chen, Z., Wei, W., Hu, Y., Yue, X., et al. (2017). Rice husk-based hierarchically porous carbon and magnetic particles composites for highly efficient electromagnetic wave attenuation. *J. Mat. Chem. C Mat.* 5 (19), 4695–4705. doi:10.1039/c7tc00987a

Fang, Y.-S., Yuan, J., Liu, T. T., Wang, Q. Q., Cao, W. Q., and Cao, M. S. (2022). Clipping electron transport and polarization relaxation of Ti3C2Tx based nanocomposites towards multifunction. *Carbon* 201, 371–380. doi:10.1016/j.carbon.2022.09.043

Gabal, M. A., Katowah, D. F., Hussein, M. A., Al-Juaid, A. A., Awad, A., Abdel-Daiem, A. M., et al. (2021). Structural and magnetoelectrical properties of MFe_2O_4 (M = Co, Ni, Cu, Mg, and Zn) ferrospinels synthesized via an egg-white biotemplate. *ACS Omega* 6 (34), 22180–22187. doi:10.1021/acsomega.1c02858

Gao, R., Liu, B., and Xu, Z. (2019). Fabrication of magnetic zeolite coated with carbon fiber using pyrolysis products from waste printed circuit boards. *J. Clean. Prod.* 231, 1149–1157. doi:10.1016/j.jclepro.2019.05.220

Gao, S., An, Q., Xiao, Z., Zhai, S., and Shi, Z. (2018). Significant promotion of porous architecture and magnetic Fe_3O_4 NPs inside honeycomb-like carbonaceous composites for enhanced microwave absorption. *RSC Adv.* 8 (34), 19011–19023. doi:10.1039/c8ra00913a

Gou, G., Meng, F., Wang, H., Jiang, M., Wei, W., and Zhou, Z. (2019). Wheat straw-derived magnetic carbon foams: *In-situ* preparation and tunable high-performance microwave absorption. *Nano Res.* 12 (6), 1423–1429. doi:10.1007/s12274-019-2376-x

Guo, H.-L., Wang, X. F., Qian, Q. Y., Wang, F. B., and Xia, X. H. (2009). A green approach to the synthesis of graphene nanosheets. *ACS Nano* 3 (9), 2653–2659. doi:10.1021/nn900227d

Guo, L., Gao, S. S., An, Q. D., Xiao, Z. Y., Zhai, S. R., Yang, D. J., et al. (2019). Dopamine-derived cavities/Fe_3O_4 nanoparticles-encapsulated carbonaceous composites with self-generated three-dimensional network structure as an excellent microwave absorber. *RSC Adv.* 9 (2), 766–780. doi:10.1039/c8ra08851a

Guo, Y., Pan, L., Yang, X., Ruan, K., Han, Y., Kong, J., et al. (2019). Simultaneous improvement of thermal conductivities and electromagnetic interference shielding performances in polystyrene composites via constructing interconnection oriented networks based on electrospinning technology. *Compos. Part A Appl. Sci. Manuf.* 124, 105484. doi:10.1016/j.compositesa.2019.105484

Hou, T., Wang, B., Ma, M., Feng, A., Huang, Z., Zhang, Y., et al. (2020). Preparation of two-dimensional titanium carbide ($Ti_3C_2T_x$) and $NiCo_2O_4$ composites to achieve excellent microwave absorption properties. *Compos. Part B Eng.* 180, 107577. doi:10.1016/j.compositesb.2019.107577

Huang, X., Zhang, J., Rao, W., Sang, T., Song, B., and Wong, C. (2016). Tunable electromagnetic properties and enhanced microwave absorption ability of flaky graphite/cobalt zinc ferrite composites. *J. Alloys Compd.* 662, 409–414. doi:10.1016/j.jallcom.2015.12.076

Huang, Y., Wang, Y., Li, Z., Yang, Z., and Shen, C. (2014). Effect of pore morphology on the dielectric properties of porous carbons for microwave absorption applications. *J. Phys. Chem. C* 118 (45), 26027–26032. doi:10.1021/jp506999k

Jain, A., Balasubramanian, R., and Srinivasan, M. P. (2016). Hydrothermal conversion of biomass waste to activated carbon with high porosity: A review. *Chem. Eng. J.* 283, 789–805. doi:10.1016/j.cej.2015.08.014

Keykavous-Amand, S., and Peymanfar, R. (2021). Fabrication of clay soil/$CuFe_2O_4$ nanocomposite toward improving energy and shielding efficiency of buildings. *Sci. Rep.* 11 (1), 20832–20913. doi:10.1038/s41598-021-00347-x

Lei, Y., Yao, Z., Li, S., Zhou, J., Haidry, A. A., and Liu, P. (2020). Broadband high-performance electromagnetic wave absorption of Co-doped NiZn ferrite/polyaniline on MXenes. *Ceram. Int.* 46, 10006–10015. doi:10.1016/j.ceramint.2019.12.189

Li, J., Xie, Y., Lu, W., and Chou, T. W. (2018). Flexible electromagnetic wave absorbing composite based on 3D rGO-CNT-Fe_3O_4 ternary films. *Carbon* 129, 76–84. doi:10.1016/j.carbon.2017.11.094

Li, W., Chen, X., Zhang, Z., Wu, Z., Yang, L., and Zou, Y. (2022). Ultralight and low-cost structural absorbers with enhanced microwave absorption performance based on sustainable waste biomass. *IEEE Trans. Antennas Propag.* 70 (1), 401–409. doi:10.1109/tap.2021.3098586

Li, W., Qi, H., Guo, F., Niu, X., Du, Y., and Chen, Y. (2019). NiFe2O4 nanoparticles supported on cotton-based carbon fibers and their application as a novel broadband microwave absorbent. *RSC Adv.* 9 (51), 29959–29966. doi:10.1039/c9ra05844c

Li, X., Du, D., Wang, C., Wang, H., and Xu, Z. (2018). *In situ* synthesis of hierarchical rose-like porous Fe@C with enhanced electromagnetic wave absorption. *J. Mat. Chem. C Mat.* 6 (3), 558–567. doi:10.1039/c7tc04897a

Li, Z. J., Yu, H. Y., Song, G. Y., Zhao, J., Zhang, H., Zhang, M., et al. (2017). Ten-gram scale SiC@SiO_2 nanowires: High-yield synthesis towards industrialization, *in situ* growth mechanism and their peculiar photoluminescence and electromagnetic wave absorption properties. *Phys. Chem. Chem. Phys.* 19 (5), 3948–3954. doi:10.1039/c6cp07457j

Li, Z., Lin, H., Ding, S., Ling, H., Wang, T., Miao, Z., et al. (2020). Synthesis and enhanced electromagnetic wave absorption performances of Fe_3O_4@C decorated walnut shell-derived porous carbon. *Carbon* 167, 148–159. doi:10.1016/j.carbon.2020.05.070

Liang, C., Qiu, H., Song, P., Shi, X., Kong, J., and Gu, J. (2020). Ultra-light MXene aerogel/wood-derived porous carbon composites with wall-like "mortar/brick" structures for electromagnetic interference shielding. *Sci. Bull.* 65 (8), 616–622. doi:10.1016/j.scib.2020.02.009

Liang, H., Liu, J., Zhang, Y., Luo, L., and Wu, H. (2019). Ultra-thin broccoli-like SCFs@TiO_2 one-dimensional electromagnetic wave absorbing material. *Compos. Part B Eng.* 178, 107507. doi:10.1016/j.compositesb.2019.107507

Liu, J., Liang, H., Zhang, Y., Wu, G., and Wu, H. (2019). Facile synthesis of ellipsoid-like $MgCo_2O_4$/Co_3O_4 composites for strong wideband microwave absorption application. *Compos. Part B Eng.* 176, 107240. doi:10.1016/j.compositesb.2019.107240

Liu, Y., Wang, Q., Fang, Q., Liu, W., and Meng, F. (2022). Facile synthesis of $CoFe_2O_4$/reduced graphene oxide nanocomposites with adjusting porous morphology for efficient microwave absorption. *J. Magnetism Magnetic Mater.* 546, 168903. doi:10.1016/j.jmmm.2021.168903

Luo, H., Gong, R., Wang, X., Nie, Y., Chen, Y., and Harris, V. G. (2015). Fe_3O_4 cladding enhanced magnetic natural resonance and microwave absorption properties of Fe0.65Co0.35 alloy flakes. *J. Alloys Compd.* 646, 345–350. doi:10.1016/j.jallcom.2015.05.208

Ma, J., Wang, X., Cao, W., Han, C., Yang, H., Yuan, J., et al. (2018). A facile fabrication and highly tunable microwave absorption of 3D flower-like Co_3O_4-rGO hybrid-architectures. *Chem. Eng. J.* 339, 487–498. doi:10.1016/j.cej.2018.01.152

Mathew, D. S., and Juang, R.-S. (2007). An overview of the structure and magnetism of spinel ferrite nanoparticles and their synthesis in microemulsions. *Chem. Eng. J.* 129 (1), 51–65. doi:10.1016/j.cej.2006.11.001

Mingdong, C., Huangzhong, Y., Xiaohua, J., and Yigang, L. (2018). Optimization on microwave absorbing properties of carbon nanotubes and magnetic oxide composite materials. *Appl. Surf. Sci.* 434, 1321–1326. doi:10.1016/j.apsusc.2017.11.107

Mu, Y., Ma, Z. H., Liang, H. S., Zhang, L. M., and Wu, H. J. (2022). Ferrite-based composites and morphology-controlled absorbers. *Rare Met.* 41, 2943–2970. doi:10.1007/s12598-022-02045-7

Pang, J., Zhang, W., Zhang, H., Zhang, J., Zhang, H., Cao, G., et al. (2018). Sustainable nitrogen-containing hierarchical porous carbon spheres derived from sodium lignosulfonate for high-performance supercapacitors. *Carbon* 132, 280–293. doi:10.1016/j.carbon.2018.02.077

Pang, J., Zhang, W., Zhang, J., Cao, G., Han, M., and Yang, Y. (2017). Facile and sustainable synthesis of sodium lignosulfonate derived hierarchical porous carbons for supercapacitors with high volumetric energy densities. *Green Chem.* 19 (16), 3916–3926. doi:10.1039/c7gc01434a

Peymanfar, R., Ahmadi, A., Selseleh-Zakerin, E., Ghaffari, A., Mojtahedi, M. M., and Sharifi, A. (2021). Electromagnetic and optical characteristics of wrinkled Ni nanostructure coated on carbon microspheres. *Chem. Eng. J.* 405, 126985. doi:10.1016/j.cej.2020.126985

Peymanfar, R., Ershad, Z. S., Selseleh-Zakerin, E., and Tavassoli, S. H. (2022). Graphite-like carbon nitride (g-C_3N_4): A promising microwave absorber. *Ceram. Int.* 48, 16461–16476. doi:10.1016/j.ceramint.2022.03.314

Peymanfar, R., and Ghorbanian-Gezaforodi, S. (2021). Functionalized carbonized monarch butterfly wing scales (FCBW) ornamented by β-Co (OH) 2 nanoparticles: An investigation on its microwave, magnetic, and optical characteristics. *Nanotechnology* 32 (19), 195201. doi:10.1088/1361-6528/abe0e4

Peymanfar, R., and Ghorbanian-Gezaforodi, S. (2020). Preparation of graphite-like carbon nitride (g-C_3N_4)/$NiCo_2S_4$ nanocomposite toward salient microwave characteristics and evaluation of medium influence on its microwave features. *Nanotechnology* 31 (49), 495202. doi:10.1088/1361-6528/abb2c0

Peymanfar, R., Keykavous-Amand, S., Abadi, M. M., and Yassi, Y. (2020). A novel approach toward reducing energy consumption and promoting electromagnetic interference shielding efficiency in the buildings using Brick/polyaniline nanocomposite. *Constr. Build. Mater.* 263, 120042. doi:10.1016/j.conbuildmat.2020.120042

Peymanfar, R., and Mirkhan, A. (2022). Biomass-derived materials: Promising, affordable, capable, simple, and lightweight microwave absorbing structures. *Chem. Eng. J.* 446, 136903. doi:10.1016/j.cej.2022.136903

Peymanfar, R., and Moradi, F. (2020). Functionalized carbon microfibers (biomass-derived) ornamented by Bi_2S_3 nanoparticles: An investigation on their microwave, magnetic, and optical characteristics. *Nanotechnology* 32 (6), 065201. doi:10.1088/1361-6528/abc2ec

Peymanfar, R., Selseleh-Zakerin, E., Ahmadi, A., Saeidi, A., and Tavassoli, S. H. (2021). Preparation of self-healing hydrogel toward improving electromagnetic interference shielding and energy efficiency. *Sci. Rep.* 11 (1), 16161–16212. doi:10.1038/s41598-021-95683-3

Peymanfar, R., Selseleh-Zakerin, E., Ahmadi, A., and Tavassoli, S. H. (2021). Architecting functionalized carbon microtube/carrollite nanocomposite demonstrating significant microwave characteristics. *Sci. Rep.* 11 (1), 11932–12015. doi:10.1038/s41598-021-91370-5

Qi, X., Hu, Q., Cai, H., Xie, R., Bai, Z., Jiang, Y., et al. (2016). Heteronanostructured Co@carbon nanotubes-graphene ternary hybrids: Synthesis, electromagnetic and excellent microwave absorption properties. *Sci. Rep.* 6 (1), 37972. doi:10.1038/srep37972

Qin, M., Zhang, L., and Wu, H. (2022). Dielectric loss mechanism in electromagnetic wave absorbing materials. *Adv. Sci.* 9 (10), 2105553. doi:10.1002/advs.202105553

Qing, Y., Min, D., Zhou, Y., Luo, F., and Zhou, W. (2015). Graphene nanosheet- and flake carbonyl iron particle-filled epoxy–silicone composites as thin–thickness and wide-bandwidth microwave absorber. *Carbon* 86, 98–107. doi:10.1016/j.carbon.2015.01.002

Qiu, X., Wang, L., Zhu, H., Guan, Y., and Zhang, Q. (2017). Lightweight and efficient microwave absorbing materials based on walnut shell-derived nano-porous carbon. *Nanoscale* 9 (22), 7408–7418. doi:10.1039/c7nr02628e

Sekar, M., Pandiaraj, M., Bhansali, S., Ponpandian, N., and Viswanathan, C. (2019). Carbon fiber based electrochemical sensor for sweat cortisol measurement. *Sci. Rep.* 9 (1), 403. doi:10.1038/s41598-018-37243-w

Shamsaddin Saeed, M., Seyed-Yazdi, J., and Hekmatara, H. (2020). Fe_2O_3/Fe_3O_4/PANI/MWCNT nanocomposite with the optimum amount and uniform orientation of Fe_2O_3/Fe_3O_4 NPs in polyaniline for high microwave absorbing performance. *J. Alloys Compd.* 843, 156052. doi:10.1016/j.jallcom.2020.156052

Song, C., Yin, X., Han, M., Li, X., Hou, Z., Zhang, L., et al. (2017). Three-dimensional reduced graphene oxide foam modified with ZnO nanowires for enhanced microwave absorption properties. *Carbon* 116, 50–58. doi:10.1016/j.carbon.2017.01.077

Sung Lee, J., Myung Cha, J., Young Yoon, H., and Keun Kim, Y. (2015). Magnetic multi-granule nanoclusters: A model system that exhibits universal size effect of magnetic coercivity. *Sci. Rep.* 5 (1), 12135. doi:10.1038/srep12135

Wang, J., Nie, P., Ding, B., Dong, S., Hao, X., Dou, H., et al. (2017). Biomass derived carbon for energy storage devices. *J. Mat. Chem. A Mat.* 5 (6), 2411–2428. doi:10.1039/c6ta08742f

Wang, L., Guan, H., Hu, J., Huang, Q., Dong, C., Qian, W., et al. (2019). Jute-based porous biomass carbon composited by Fe_3O_4 nanoparticles as an excellent microwave absorber. *J. Alloys Compd.* 803, 1119–1126. doi:10.1016/j.jallcom.2019.06.351

Wang, L., Huang, M., Yu, X., You, W., Zhao, B., Liang, C., et al. (2022). Engineering polarization surface of hierarchical ZnO microspheres via spray-annealing strategy for wide-frequency electromagnetic wave absorption. *J. Mater. Sci. Technol.* 131, 231–239. doi:10.1016/j.jmst.2022.05.015

Wang, L., Shi, X., Zhang, J., Zhang, Y., and Gu, J. (2020). Lightweight and robust rGO/sugarcane derived hybrid carbon foams with outstanding EMI shielding performance. *J. Mater. Sci. Technol.* 52, 119–126. doi:10.1016/j.jmst.2020.03.029

Wang, Q., Niu, B., Han, Y., Zheng, Q., Li, L., and Cao, M. (2023). Nature-inspired 3D hierarchical structured "vine" for efficient microwave attenuation and electromagnetic energy conversion device. *Chem. Eng. J.* 452, 139042. doi:10.1016/j.cej.2022.139042

Wang, X., Pan, F., Xiang, Z., Zeng, Q., Pei, K., Che, R., et al. (2020). Magnetic vortex core-shell Fe_3O_4@C nanorings with enhanced microwave absorption performance. *Carbon* 157, 130–139. doi:10.1016/j.carbon.2019.10.030

Wang, X., Shi, G., Shi, F. N., Xu, G., Qi, Y., Li, D., et al. (2016). Synthesis of hierarchical cobalt dendrites based on nanoflake self-assembly and their microwave absorption properties. *RSC Adv.* 6 (47), 40844–40853. doi:10.1039/c6ra06112e

Wang, Y., Gao, X., Zhang, W., Luo, C., Zhang, L., and Xue, P. (2018). Synthesis of hierarchical CuS/RGO/PANI/Fe_3O_4 quaternary composite and enhanced microwave absorption performance. *J. Alloys Compd.* 757, 372–381. doi:10.1016/j.jallcom.2018.05.080

Wang, Y., Gao, X., Zhou, H., Wu, X., Zhang, W., Wang, Q., et al. (2019). Fabrication of biomass-derived carbon decorated with $NiFe_2O_4$ particles for broadband and strong microwave absorption. *Powder Technol.* 345, 370–378. doi:10.1016/j.powtec.2019.01.025

Wei, Y., Shi, Y., Jiang, Z., Zhang, X., Chen, H., Zhang, Y., et al. (2019). High performance and lightweight electromagnetic wave absorbers based on TiN/RGO flakes. *J. Alloys Compd.* 810, 151950. doi:10.1016/j.jallcom.2019.151950

Wu, H., Wu, G., and Wang, L. (2015). Peculiar porous α-Fe_2O_3, γ-Fe_2O_3 and Fe_3O_4 nanospheres: Facile synthesis and electromagnetic properties. *Powder Technol.* 269, 443–451. doi:10.1016/j.powtec.2014.09.045

Wu, Z., Meng, Z., Yao, C., Deng, Y., Zhang, G., and Wang, Y. (2022). Rice husk derived hierarchical porous carbon with lightweight and efficient microwave absorption. *Mater. Chem. Phys.* 275, 125246. doi:10.1016/j.matchemphys.2021.125246

Wu, Z., Tian, K., Huang, T., Hu, W., Xie, F., Wang, J., et al. (2018). Hierarchically porous carbons derived from biomasses with excellent microwave absorption performance. *ACS Appl. Mat. Interfaces* 10 (13), 11108–11115. doi:10.1021/acsami.7b17264

Xi, J., Zhou, E., Liu, Y., Gao, W., Ying, J., Chen, Z., et al. (2017). Wood-based straightway channel structure for high performance microwave absorption. *Carbon* 124, 492–498. doi:10.1016/j.carbon.2017.07.088

Xie, X., Wang, B., Wang, Y., Ni, C., Sun, X., and Du, W. (2022). Spinel structured MFe_2O_4 (M = Fe, Co, Ni, Mn, Zn) and their composites for microwave absorption: A review. *Chem. Eng. J.* 428, 131160. doi:10.1016/j.cej.2021.131160

Xie, X., Wang, Y., Sun, X., Wang, H., Yu, R., Du, W., et al. (2023). Optimizing impedance matching by a dual-carbon Co-regulation strategy of Co_3O_4@ rGO/celery stalks derived carbon composites for excellent microwave absorption. *J. Mater. Sci. Technol.* 133, 1–11. doi:10.1016/j.jmst.2022.05.058

Yan, J., Huang, Y., Han, X., Gao, X., and Liu, P. (2019). Metal organic framework (ZIF-67)-derived hollow CoS_2/N-doped carbon nanotube composites for extraordinary electromagnetic wave absorption. *Compos. Part B Eng.* 163, 67–76. doi:10.1016/j.compositesb.2018.11.008

Yan, X., Guo, J., and Jiang, X. (2022). The microwave-absorption properties and mechanism of phenyl silicone rubber/CIPs/graphene composites after thermal-aging in an elevated temperature. *Sci. Rep.* 12 (1), 4385. doi:10.1038/s41598-022-08415-6

Yang, B., Fang, J., Xu, C., Cao, H., Zhang, R., Zhao, B., et al. (2022). One-dimensional magnetic FeCoNi alloy toward low-frequency electromagnetic wave absorption. *Nanomicro. Lett.* 14 (1), 170–213. doi:10.1007/s40820-022-00920-7

Yang, L., Cai, H., Zhang, B., Huo, S., and Chen, X. (2018). Enhanced microwave absorption property of epoxy nanocomposites based on PANI@Fe_3O_4@CNFs nanoparticles with three-phase heterostructure. *Mat. Res. Express* 5 (2), 025304. doi:10.1088/2053-1591/aaab8d

Yang, T., Qian, T., Wang, M., Shen, X., Xu, N., Sun, Z., et al. (2016). A sustainable route from biomass byproduct okara to high content nitrogen-doped carbon sheets for efficient sodium ion batteries. *Adv. Mat.* 28 (3), 539–545. doi:10.1002/adma.201503221

Yu, L., Zhu, Y., and Fu, Y. (2018). Waxberry-like carbon@polyaniline microspheres with high-performance microwave absorption. *Appl. Surf. Sci.* 427, 451–457. doi:10.1016/j.apsusc.2017.08.078

Yun, X., Wu, Q., Feng, L., Shen, J., Chen, J., Chu, P. K., et al. (2020). Microwave absorption enhancement of e-Fe_3O_4@C microspheres by core surface modification. *J. Alloys Compd.* 835, 155307. doi:10.1016/j.jallcom.2020.155307

Zhang, F., Cui, W., Wang, B., Xu, B., Liu, X., Liu, X., et al. (2021). Morphology-control synthesis of polyaniline decorative porous carbon with remarkable electromagnetic wave absorption capabilities. *Compos. Part B Eng.* 204, 108491. doi:10.1016/j.compositesb.2020.108491

Zhang, M., Zhang, J., Lin, H., Wang, T., Ding, S., Li, Z., et al. (2020). Designable synthesis of reduced graphene oxide modified using $CoFe_2O_4$ nanospheres with tunable enhanced microwave absorption performances between the whole X and Ku bands. *Compos. Part B Eng.* 190, 107902. doi:10.1016/j.compositesb.2020.107902

Zhang, X., Ji, G., Liu, W., Quan, B., Liang, X., Shang, C., et al. (2015). Thermal conversion of an Fe_3O_4@metal–organic framework: A new method for an efficient Fe–Co/nanoporous carbon microwave absorbing material. *Nanoscale* 7 (30), 12932–12942. doi:10.1039/c5nr03176a

Zhang, Y., Huang, Y., Zhang, T., Chang, H., Xiao, P., Chen, H., et al. (2015). Broadband and tunable high-performance microwave absorption of an ultralight and highly compressible graphene foam. *Adv. Mat.* 27 (12), 2049–2053. doi:10.1002/adma.201405788

Zhang, Y., Meng, H., Shi, Y., Zhang, X., Liu, C., Wang, Y., et al. (2020). TiN/Ni/C ternary composites with expanded heterogeneous interfaces for efficient microwave absorption. *Compos. Part B Eng.* 193, 108028. doi:10.1016/j.compositesb.2020.108028

Zhao, B., Deng, J., Zhao, C., Wang, C., Chen, Y. G., Hamidinejad, M., et al. (2020). Achieving wideband microwave absorption properties in PVDF nanocomposite foams with an ultra-low MWCNT content by introducing a microcellular structure. *J. Mat. Chem. C Mat.* 8 (1), 58–70. doi:10.1039/c9tc04575a

Zhou, M., Wang, J., Wang, G., Zhao, Y., Tang, J., Pan, J., et al. (2022). Lotus leaf-inspired and multifunctional Janus carbon felt@ Ag composites enabled by *in situ* asymmetric modification for electromagnetic protection and low-voltage joule heating. *Compos. Part B Eng.* 242, 110110. doi:10.1016/j.compositesb.2022.110110

Zhou, P., Wang, X., Wang, L., Zhang, J., Song, Z., Qiu, X., et al. (2019). Walnut shell-derived nanoporous carbon@Fe_3O_4 composites for outstanding microwave absorption performance. *J. Alloys Compd.* 805, 1071–1080. doi:10.1016/j.jallcom.2019.07.177

Zickler, G. A., Smarsly, B., Gierlinger, N., Peterlik, H., and Paris, O. (2006). A reconsideration of the relationship between the crystallite size La of carbons determined by X-ray diffraction and Raman spectroscopy. *Carbon* 44 (15), 3239–3246. doi:10.1016/j.carbon.2006.06.029

Zong, M., Huang, Y., Zhao, Y., Sun, X., Qu, C., Luo, D., et al. (2013). Facile preparation, high microwave absorption and microwave absorbing mechanism of RGO–Fe_3O_4 composites. *RSC Adv.* 3 (45), 23638–23648. doi:10.1039/c3ra43359e